

# An Ocean Modeling Study To Quantify Wind Forcing and Oceanic Mixing Effects on The Tropical North Pacific Subsurface Warm Bias in CMIP and OMIP Simulations

Yuchao Zhu

Institute of Oceanology Chinese Academy of Sciences

Rong-Hua Zhang (✉ [rzhang@qdio.ac.cn](mailto:rzhang@qdio.ac.cn))

Institute of Oceanology, Chinese Academy of Sciences <https://orcid.org/0000-0002-3332-7849>

Delei Li

Institute of Oceanology Chinese Academy of Sciences

---

## Research Article

**Keywords:** Model errors, Subsurface temperature bias, CMIP/OMIP simulations, Vertical mixing scheme, Wind forcing errors

**Posted Date:** February 18th, 2021

**DOI:** <https://doi.org/10.21203/rs.3.rs-204857/v1>

**License:** © ⓘ This work is licensed under a Creative Commons Attribution 4.0 International License.

[Read Full License](#)

---

**Version of Record:** A version of this preprint was published at Climate Dynamics on September 5th, 2021. See the published version at <https://doi.org/10.1007/s00382-021-05946-y>.

1           **An ocean modeling study to quantify wind forcing and oceanic**  
2           **mixing effects on the tropical North Pacific subsurface warm bias in**  
3                           **CMIP and OMIP simulations**

4  
5                           Yuchao Zhu<sup>1,2</sup>, Rong-Hua Zhang\*<sup>1,2,3,4</sup> and Delei Li<sup>1,2</sup>

6  
7           <sup>1</sup>CAS Key Laboratory of Ocean Circulation and Waves, Institute of Oceanology, and Center for  
8           Ocean Mega-Science, Chinese Academy of Sciences, Qingdao, 266071, China;

9           <sup>2</sup>Pilot National Laboratory for Marine Science and Technology (Qingdao), Qingdao, China;

10          <sup>3</sup>Center for Excellence in Quaternary Science and Global Change, Chinese Academy of Sciences,  
11          Xian 710061, China;

12          <sup>4</sup>University of Chinese Academy of Sciences, Beijing, China;

13  
14  
15  
16  
17  
18           

---

  
19           *Corresponding author address:*

20           Rong-Hua Zhang, Key Laboratory of Ocean Circulation and Waves, Institute of Oceanology,

21           Chinese Academy of Sciences, Qingdao 266071, China

22           Email: [rzhang@qdio.ac.cn](mailto:rzhang@qdio.ac.cn)

## Abstract

23  
24 Sea surface temperature (SST) bias in the climate models has been a  
25 focus in the past, but subsurface temperature biases have not been received  
26 much attention yet. In this study, subsurface temperature biases in the  
27 Tropical North Pacific (TNP) are investigated by analyzing the CMIP6,  
28 CMIP5 and OMIP products, and performing ocean model simulations. It is  
29 found that almost all the CMIP and OMIP simulations have a pronounced  
30 subsurface warm bias (SWB) in the northeastern tropical Pacific (NETP),  
31 and the model developments over the past decade do not indicate obvious  
32 improvements in bias pattern and magnitude from CMIP5 to the latest  
33 version CMIP6. This SWB is primarily caused by the model deficiencies  
34 in the simulated surface wind stress curl (WSC) in the NETP, which is too  
35 weak to produce a sufficient Ekman upwelling, a bias that also exists in  
36 OMIP simulations. The uncertainties in the parameterizations of the  
37 oceanic vertical mixing processes also make a great contribution, and it is  
38 demonstrated that the estimated oceanic vertical diffusivities are  
39 overestimated both in the upper boundary layer and the interior in the  
40 CMIP and OMIP simulations. The relationship between the SWB and the  
41 misrepresented oceanic vertical mixing processes are investigated by  
42 conducting several ocean-only experiments, in which the upper boundary  
43 layer mixing is modified by reducing the wind stirring effect in the Kraus-  
44 Turner type bulk mixed-layer approach, and the interior mixing is

45 constrained by using the Argo-derived diffusivity. By applying these  
46 modifications to oceanic vertical mixing schemes, the SWB is greatly  
47 reduced in the NETP. The consequences of this SWB are further analyzed.  
48 Because the thermal structure in the NETP can influence the simulations  
49 of oceanic circulations and equatorial upper-ocean thermal structure, the  
50 large SWB in the CMIP6 models tends to produce a weak equatorward  
51 water transport in the subsurface TNP, a weak equatorial upwelling and a  
52 warm equatorial upper ocean.

53 **Keywords:** Model errors; Subsurface temperature bias; CMIP/OMIP  
54 simulations; Vertical mixing scheme; Wind forcing errors

55

56 **1. Introduction**

57       Understanding climate model biases is critically important for the  
58 assessments of future climate change, and hence “What are the origins and  
59 consequences of systematic model biases?” is one of the three key  
60 scientific issues have been addressed in CMIP6 (Eyring et al., 2016). Given  
61 the important role played by sea surface temperature (SST) in air-sea  
62 coupling, SST biases in climate models have received considerable  
63 attention in the past. For example, the too cold tongue bias along the  
64 equatorial Pacific can be attributed to the misrepresented oceanic vertical  
65 turbulent mixing processes along the equator (Jochum, 2009; Sasaki et al.,  
66 2013; Furue et al., 2015; Jia et al., 2015; Zhu and Zhang, 2018b, 2019),  
67 overestimated cloud albedo in the subtropics (Burls et al., 2017; Thomas  
68 and Fedorov, 2017), uncertainties in the atmospheric convection  
69 parameterizations (Woelfle et al., 2018), and so on. The warm SST bias in  
70 the southeastern tropical Pacific and Atlantic can be attributed to coarse  
71 resolutions of climate models (Seo et al., 2006; Small et al., 2014),  
72 uncertainties in the parameterizations of atmospheric convection and cloud  
73 physics (Ma et al., 1996; Gordon et al., 2000), and eastward propagation  
74 of equatorial subsurface warm bias (Xu et al., 2014). SST biases can  
75 severely degrade the credibility of climate predictions and projections. For  
76 example, too cold tongue bias in the equatorial Pacific promotes a La Niña-  
77 like warming pattern in the tropical Pacific under the increasing

78 concentrations of greenhouse gases, whereas an El Niño-like warming  
79 pattern is produced when the too cold tongue bias is removed from model  
80 projections (Li et al., 2016; Ying et al., 2019).

81 Thermal structure and variability in the subsurface oceans are known  
82 to play an important role in the climate change. For example, the  
83 acceleration of ocean subsurface warming and the slowdown of surface  
84 warming in the early decade of the 21st century indicate that deep oceans  
85 play a critical role in regulating the global warming (Chen and Tung, 2014;  
86 Wang et al., 2018). However, compared with that at sea surface,  
87 temperature bias in the subsurface oceans is poorly understood. Therefore,  
88 it is essential to investigate the oceanic subsurface temperature bias for  
89 understanding the simulations and predictions of global energy and heat  
90 redistribution. Particularly, subsurface temperature simulation in the  
91 tropics is very important to the climate simulations. For instance, Xu et al.  
92 (2014) find that the subsurface warm bias within the Atlantic equatorial  
93 thermocline can be transported to the Benguela coast by horizontal currents  
94 and subsequently surfaces by coastal upwelling, contributing to the  
95 longstanding warm SST bias in the eastern tropical Atlantic. In addition,  
96 subsurface warm temperature bias along the Pacific equator generates a too  
97 diffuse equatorial thermocline, leading to a weak SST-thermocline  
98 feedback in the tropical air-sea coupling (Guilyardi et al., 2009; Gao and  
99 Zhang, 2017; Zhang et al., 2020). Off the equator, subsurface temperature

100 bias in the climate models is of the opposite sign in the north and south  
101 tropical Pacific: a large warm bias between 5°-10° N and a large cold bias  
102 near 10° S (Wittenberg et al., 2006; Zhu et al., 2020a). Though being  
103 substantial in its magnitude, the subsurface temperature bias off the equator  
104 has not been receive much attention yet. Importantly, owing to the local  
105 Ekman pumping in the Tropical North Pacific (TNP), climatological  
106 pycnocline tends to arise to form a potential vorticity barrier, acting to  
107 block the local water exchange between the subtropics and tropics (Lu and  
108 McCreary, 1995; Rothstein et al., 1998; Johnson and McPhaden, 1999). In  
109 this way, the subsurface warm bias in the TNP acts to weaken the potential  
110 vorticity barrier, and would affect the width of subtropical-tropical water  
111 exchange window.

112       Subsurface temperature bias also reflects an erroneous representation  
113 of oceanic vertical heat distribution in climate models. Thus, in addition to  
114 the poorly simulated atmospheric forcing, flaws in ocean models might be  
115 an important source of subsurface temperature bias. One simulation flaw  
116 is associated with the oceanic mesoscale eddies, which act to transport heat  
117 upward and offset the downward heat transport; these processes are  
118 unsolved in coarse resolution models. By increasing the ocean model  
119 resolution to the eddy resolving level, subsurface warm bias in the  
120 subtropical gyres can be reduced (Griffies et al., 2015; Rackow et al., 2019).  
121 Besides, ocean simulations are very sensitive to the parameterizations

122 representing the oceanic vertical turbulent mixing. For example, an  
123 overestimated vertical mixing by strong vertical shear is responsible for the  
124 subsurface warm bias in the tropical Indian Ocean (Chowdary et al., 2016),  
125 and a salty and warm bias in Antarctic Intermediate Water simulations is  
126 largely caused by the misrepresentation of oceanic mixing processes (Zhu  
127 et al., 2018).

128       Based on the previous studies, we will continue to investigate the  
129 subsurface temperature bias in the TNP, focusing mainly on the bias  
130 contributions from the atmospheric wind forcing fields and the oceanic  
131 vertical mixing parameterization by performing CMIP-based analyses and  
132 ocean model-based experiments. This paper is organized as follows.  
133 Section 2 describes the datasets from CMIP simulations, reanalysis and  
134 observational products for model evaluation, and model configurations for  
135 MOM5-based numerical experiments. Section 3 describes the  
136 characteristics of subsurface temperature biases in the TNP. Atmospheric  
137 and oceanic origins of the subsurface temperature biases are investigated  
138 in Section 4 and Section 5, respectively. The influences of the temperature  
139 biases on the upper-ocean thermal and current structures are discussed in  
140 Section 6. Finally, summaries and discussions are given in Section 7.

141

## 142 **2. Datasets and ocean model used**

143       This study is primarily based on the historical simulations from 53

144 CMIP6 models (Eyring et al., 2016), which are available online at  
145 <https://esgf-node.llnl.gov/projects/cmip6/>. The historical simulations are  
146 forced by the observed greenhouse gases, solar forcing, and volcanic  
147 aerosols from 1850-2014, providing an opportunity to evaluate model  
148 abilities to simulate the past climate. In our analysis, the last 35 years  
149 (1980-2014) of historical simulations are selected for model evaluations.  
150 All the selected CMIP6 outputs are interpolated onto a 1° horizontal grid,  
151 and the potential temperature fields are further interpolated to 87 standard  
152 levels with a vertical resolution of 10 m near the sea surface. As we are  
153 interested in the long-term mean biases in climate simulations, the mean  
154 states for all fields are calculated by averaging the entire selected period.  
155 In addition, 41 CMIP5 models and 16 Ocean Model Intercomparison  
156 Project (OMIP) (Griffies et al., 2016) models are also used in our study.  
157 All the models are listed in Table 1.

158 In order to evaluate the subsurface temperature biases in CMIP6  
159 simulations, the EN4 objective analyses of subsurface temperature from  
160 the Met Office Hadley Centre are used (Good et al., 2013). The EN4  
161 product consists of temperature and salinity fields from 1900 to the present,  
162 with a 1° horizontal resolution and 42 vertical levels. In addition, wind  
163 stress fields are taken from the fifth generation of ECMWF atmospheric  
164 reanalyses (ERA5; Copernicus Climate Change Service, 2017) and the  
165 Scatterometer Climatology of Ocean Winds (SCOW); the latter is

166 estimated from the 122-month record of the QuikSCAT wind  
167 measurements (Risien and Chelton, 2008).

168 Bias quantification is made by conducting the MOM5-based ocean-  
169 only experiments (Griffies et al., 2009). This ocean model has a  $1^\circ$   
170 horizontal resolution with the meridional resolution increased to  $1/3$  near  
171 the equator, and 50 vertical levels with 10 m resolution in the upper 220 m.  
172 In order to investigate the relationship between the subsurface temperature  
173 bias in the TNP and the poorly prescribed atmospheric forcing fields, two  
174 ocean-only simulations are conducted. In the control run (the LY09 run),  
175 the Normal Year atmospheric forcing fields from Large and Yeager (2009),  
176 which are the required forcing fields by OMIP (Eyring et al., 2016), is  
177 applied. While in the sensitivity run (the ERA5 run), forcing field of wind  
178 is replaced by ERA5. Furthermore, in order to investigate the relationship  
179 between the subsurface temperature bias in the TNP and the parameterized  
180 oceanic vertical mixing processes, several ocean-only experiments are  
181 conducted, in which mixing strength in the upper ocean and the interior  
182 ocean is reduced. Specifically, the upper boundary layer mixing is modified  
183 by reducing the wind stirring effect in a Kraus-Turner type mixing scheme  
184 (Chen et al., 1994), and the interior mixing is constrained by using the  
185 Argo-derived diffusivity (Zhu and Zhang, 2018a), whose details are given  
186 in Section 5.

187

### 188 **3. Subsurface temperature bias in the TNP**

189        In the northeastern tropical Pacific (NETP), a subsurface warm bias  
190 (SWB) emerges in most of CMIP6 simulations, with its bias center located  
191 near (10° N, 130° W) at the depth of 100 m (Fig. 1a). The multimodel mean  
192 bias is about 4 °C with the maximum greater than 8 °C (Fig. 1b). Although  
193 great efforts have been made to improve climate model performances over  
194 the past decade, the SWB in the NETP has not been reduced significantly  
195 from CMIP5 to CMIP6 (Fig. 2). Figure 3 shows the seasonal variation of  
196 the SWB. Warm bias is large during April-June, and is relatively small  
197 during boreal winter, accompanied by a deep thermocline bias throughout  
198 the year.

199        This SWB is located in an important region where a positive wind  
200 stress curl (WSC) produces a positive Ekman pumping near the  
201 Intertropical Convergence Zone (ITCZ). As a consequence, a ridge-like  
202 climatological thermocline arises to form a potential vorticity barrier  
203 blocking the local water exchange between the subtropics and tropics (Lu  
204 and McCreary, 1995; Johnson and McPhaden, 1999). Therefore, WSC over  
205 the NETP might be underestimated by CMIP6 models, and the consequent  
206 Ekman upwelling is too weak to maintain the shallow thermocline as  
207 observed. In the next section, the relationship between the SWB and the  
208 wind stress simulations is examined.

209

#### 210 **4. The contribution of surface wind stress to SWB**

211 Figure 4a shows the linear regression of the intermodel WSC onto the  
212 normalized SWB series (Fig. 1b). The NETP happens to be the region  
213 where negative regression coefficients arise. As the weak WSC tends to  
214 produce a weak Ekman upwelling, intermodel differences in SWB are  
215 largely explained by the differences in the simulation of local WSC.  
216 However, whether the WSC intensity in the NETP is underestimated by  
217 CMIP6 models is quite uncertain. Figure 4b shows the annual-mean WSC  
218 difference between the CMIP6 multimodel ensemble (MME) and the  
219 ERA5. It seems plausible that the WSC intensity in the NETP is indeed  
220 underestimated by CMIP6 models when the wind fields in ERA5 are  
221 considered to be realistic. But it is widely accepted that wind measurements  
222 by QuikSCAT are more reliable, and so the QuikSCAT winds are widely  
223 used to correct the atmospheric reanalyses winds (Large and Yeager, 2009;  
224 Tsujino et al., 2018). Figure 4c shows the WSC difference between the  
225 CMIP6 MME and the SCOW. It is obvious that the positive WSC  
226 difference extends farther south, almost occupying the entire  $10^{\circ}$  N. Hence,  
227 the WSC bias in the NETP is positive rather than negative when the  
228 QuikSCAT measurements are considered to be more realistic than ERA5.

229 However, the reliability of the QuikSCAT measurements has been  
230 questioned. Many previous studies have found that the accuracy of the  
231 QuikSCAT measurements can be degraded by rain (Weissman et al., 2002;

232 Draper and Long, 2004; Sun et al., 2019). Therefore, the WSC in the ITCZ  
233 region can be poorly measured by the QuikSCAT, and correcting the  
234 reanalysis winds towards the QuikSCAT winds might introduce a large  
235 error. Nevertheless, the forcing fields of wind in OMIP experiments just  
236 come from the NCEP and JRA55 wind fields corrected by the QuikSCAT  
237 measurements (Griffies et al., 2016). Thus, it is not surprising that this  
238 SWB also exists in the OMIP simulations (Fig. 5). To further investigate  
239 the relationship between the SWB and the wind forcing fields, two MOM5-  
240 based ocean-only experiments are conducted. In the LY09 run, the  
241 prescribed wind forcing fields are the same as those in the OMIP  
242 experiments. In the ERA5 run, ERA5 analysis winds are used to drive the  
243 ocean model. Both runs are integrated for 30 years and the outputs for the  
244 last 5-year are chosen to calculate the mean state. Figure 6 shows the  
245 temperature differences between the ERA5 run and the LY09 run.  
246 Compared with that in the LY09 run (Fig. 6a), the SWB is greatly reduced  
247 by  $\sim 6$  °C in the ERA5 run (Fig. 6c), implying that the failure of reproducing  
248 the subsurface temperature distribution in the tropical North Pacific is due  
249 to the poorly prescribed wind forcing fields in OMIP experiments.

250 Although the above analyses confirm a significant contribution of the  
251 wind stress simulations to the SWB in the NETP, its quantitative  
252 contribution is still unknown as it is difficult to obtain the accurate wind  
253 measurements and to realistically describe the WSC distributions in the

254 tropics for ocean modeling. Here, we further discuss the possible  
255 mechanisms impacting the wind simulations in the NETP. As shown in  
256 Figure 7, the SWB is closely related to the northeasterly wind in the NETP,  
257 which helps to produce a negative WSC on its right flank (Fig. 4a). Song  
258 and Zhang (2020) have found that the climate models fail to reproduce the  
259 seasonal wind reversal of the North American monsoon, leading to a year-  
260 round northeasterly wind bias in the NETP. Consistent with their study,  
261 Figure 7 shows positive regression coefficients between the sea level  
262 pressure and the SWB over the North America. Thus, the overestimated  
263 sea level pressure over the North America acts to produce a year-round  
264 northeasterly wind bias in the NETP, which further causes a negative WSC  
265 bias on its right flank. This negative WSC bias acts to suppress the local  
266 Ekman upwelling, leading to the emergence of the SWB in the NETP as  
267 represented in the CMIP simulations.

268

## 269 **5. The contribution of oceanic vertical mixing scheme to SWB**

270 Apart from the erroneous simulations in atmospheric state, the  
271 deficiencies in ocean models can also contribute to the SWB in the NETP.  
272 One of the largest sources of errors in ocean models is the  
273 parameterizations of the vertical turbulent mixing processes in the upper  
274 ocean, and the ocean simulations are very sensitive to the vertical  
275 diffusivity estimated by vertical mixing schemes. Over the past two

276 decades, three microstructure observations (Thurnherr and Laurent, 2011;  
 277 Cheng and Kitade, 2014; Fernández-Castro et al., 2014) are conducted in  
 278 the NETP (Fig. 8), providing an opportunity to assess the ability of vertical  
 279 mixing schemes in reproducing the observed mixing strength. Different  
 280 from what is observed, the estimated vertical diffusivity in ocean models  
 281 is misrepresented in the vertical: In the ocean boundary layer, the intense  
 282 vertical mixing penetrates too deep, and in the ocean interior, vertical  
 283 diffusivity is overestimated by an order of magnitude (Fig. 9, see also the  
 284 Fig. 5b in Cheng and Kitade (2014) or the Fig. 5 in Fernández-Castro et al.  
 285 (2014)).

286 The overly strong penetration of the ocean boundary layer mixing  
 287 tends to warm the subsurface layer. Thus, sensitivity experiments are  
 288 conducted to investigate the relationship between the SWB in NETP and  
 289 the overly strong mixing effect. In this subsection, a Kraus-Turner-type  
 290 vertical mixing scheme (Niiler, 1977; Chen et al., 1994) is applied to  
 291 determine the mixed layer depth as follows:

$$292 \quad \Delta b w_e h = 2m_0 u_*^3 + \frac{[(1+n)B_0 - (1-n)|B_0|]h}{2} + J_0 \left[ h(1 + e^{-h/h_p}) - 2h_p(1 - e^{-h/h_p}) \right] \quad (1)$$

293 where  $\Delta b$  is the buoyancy jump across the base of ocean surface  
 294 boundary layer,  $w_e = \partial h / \partial t$  is the entrainment velocity,  $h$  is the depth of  
 295 ocean surface boundary layer,  $u_*$  is the friction velocity,  $B_0$  and  $J_0$  are the  
 296 non-penetrating and penetrating components of the surface buoyancy flux,  
 297 and  $h_p$  is the attenuation depth of shortwave radiation in the upper ocean.

298 Here,  $m_0$  is a parameter to scale the wind stirring effect;  $n$  is a parameter to  
 299 represent the ratio of entrainment buoyancy flux to surface buoyancy flux  
 300 when convection occurs. Traditionally, constant values with  $m_0 = 0.4$  and  
 301  $n = 0.18$  are taken in ocean modelling, but some previous studies find that  
 302  $m_0$  is spatially varying with values less than 0.4 in the NETP (Acreman and  
 303 Jeffery, 2007; Zhu and Zhang, 2018a). This prognostic equation of  $h$  has  
 304 been employed into MOM5 to depict the evolution of ocean surface  
 305 boundary layer. When the  $h$  is determined by the equation (1), vertical  
 306 mixing coefficients for the model layers within the  $h$  are assigned to be a  
 307 constant value of  $5 \times 10^{-3} \text{ m}^2 \text{ s}^{-1}$ , the maximum observed diffusivity  
 308 reported by Peters et al. (1988). Thus, the overly deep penetration of  
 309 boundary layer mixing demonstrated in Figure 9 can be relieved by  
 310 reducing the  $m_0$  in the equation (1). Two MOM5 based ocean-only  
 311 simulations are thus conducted:  $m_0 = 0.4$  is taken in the control run; in the  
 312 reduced  $m_0$  run, the  $m_0$  is prescribed as

$$313 \quad 0.4 \times \left( 1 - \exp \left( - \left( \frac{\text{lon} - 130^\circ \text{W}}{20^\circ} \right)^2 \right) \cdot \exp \left( - \left( \frac{\text{lat} - 11^\circ \text{N}}{4^\circ} \right)^2 \right) \right) \quad (2)$$

314 in which “*lon*” and “*lat*” are the longitude and latitude of a model grid point.  
 315 Both runs are integrated for 30 years using the atmospheric climatological  
 316 forcing fields from LY09, and the outputs for the last 5 years are selected  
 317 for comparisons.

318 Figure 10a shows the annual-mean difference in ocean surface  
 319 boundary layer depth between the reduced  $m_0$  run and the control run. In

320 accord with equation (2), surface boundary layer shoals by  $\sim 15$  m in the  
321 NETP when the  $m_0$  is reduced, roughly removing the too deep surface  
322 boundary layer depth bias in Figure 9b. As a consequence, subsurface layer  
323 cools by  $\sim 1$  °C in the NETP (Fig. 10b). Moreover, the SWB is found to be  
324 more pronounced during the first half of a year (Fig. 6b). By reducing the  
325 penetration depth of the boundary layer mixing, improvements in the  
326 subsurface temperature simulations are much substantial in the reduced  $m_0$   
327 run during the first half of a year (Fig. 10c), revealing that the overly strong  
328 penetration of the mixing effect and the ocean surface boundary layer  
329 deepening indeed contribute to the SWB in the NETP.

330 Besides the misrepresented boundary layer mixing, the overestimated  
331 vertical mixing in the ocean interior may also contribute to the SWB in the  
332 NETP by inhibiting the downward heat transport to the deeper ocean.  
333 Indeed, the spatial pattern of diapycnal mixing in the tropical Pacific  
334 inferred from the strain-based finescale parameterization (Kunze et al.,  
335 2006) also confirms the weak mixing strength in the NETP for observations,  
336 coinciding with the location of the SWB (Fig. 11a). Thus similar to our  
337 previous studies (Zhu and Zhang, 2018a; Zhu et al., 2020b), two ocean-  
338 only experiments are conducted to investigate the relationship between the  
339 SWB and diapycnal mixing intensity in the NETP. In the control run,  
340 background diffusivity is taken as the commonly used value ( $10^{-5} \text{ m}^2 \text{ s}^{-1}$ ),  
341 a value that is considered to be too large compared to what is observed. In

342 the reduced background diffusivity (RBD) run considering the observed  
343 weak diapycnal mixing, background diffusivity over the NETP is replaced  
344 by the Argo-derived one (Fig. 11a). Two runs are integrated for 30 years  
345 using the LY09 forcing fields. The temperature differences averaged over  
346 the last 5 years are shown in Figure 11b and 11c, revealing that the SWB  
347 can be reduced when constraining the background diffusivity to match  
348 what is observed.

349 So, our modeling experiments clearly demonstrate that the  
350 uncertainties in the oceanic vertical mixing parameterization can produce  
351 a  $\sim 3$  °C warm bias, and the poorly simulated wind stress fields (Fig. 6c)  
352 can cause a  $\sim 6$  °C warm bias. Putting together, these two effects could  
353 account for the magnitude of SWB in coupled simulations. Although this  
354 warm bias occupies a small domain of the tropical Pacific basin, its  
355 influences might be widespread as the upper-ocean thermal structures in  
356 the TNP control the subtropical-tropical water exchanges. In the next  
357 section, some local and remote consequences of the SWB are further  
358 discussed.

359

## 360 **6. The consequences of the SWB**

361 In order to investigate the relationships between the SWB and the  
362 simulated oceanic circulations pathways in CMIP6 outputs, we define two  
363 model groups according to the magnitude of SWB (Fig. 12a): 14 models

364 are seen to have large SWB (Group1), and 10 models are seen to have  
365 trivial or little SWB (Group2). As shown in Figure 12b-12d, the CMIP6  
366 models with a large SWB in the NETP tend to produce much flatter  
367 isopycnals over the central TNP, which acts to reduce interior water  
368 transport. As a consequence, the equatorward water transport at 50-150 m  
369 in the western-central TNP is weaker than that in the models with a small  
370 SWB. Furthermore, the equatorward water transport in the subsurface TNP  
371 regulates the supply of cold water that upwells along the equator, which  
372 can be associated with the decadal changes in SST over the central and  
373 eastern equatorial Pacific (McPhaden and Zhang, 2002; Capotondi et al.,  
374 2005). Figure 13a and 13b contrast the equatorial Pacific upwelling  
375 simulated in Group1 and Group2. Consistent with our understanding of  
376 subtropical-tropical water exchange, models with the large SWB tend to  
377 produce a weak equatorial upwelling (Fig. 13c). Thus, the cooling effect  
378 by the equatorial upwelling in Group1 is weak, and the upper-ocean  
379 temperature difference between Group1 and Group2 is positive (Fig. 14a).  
380 Figure 14b shows the scatterplots of the SWB versus the equatorial Pacific  
381 upper-ocean temperature among the 53 CMIP6 models. Obviously, these  
382 two quantities show a positive correlation ( $R=0.75$ ), indicating that the  
383 CMIP6 models with the larger SWB in the NETP tend to produce a warmer  
384 equatorial upper-ocean.

385

## 386 **7. Summary and discussion**

387 Thermal structure and variability in the subsurface oceans are known  
388 to play an important role in the climate change, and the studies of oceanic  
389 subsurface temperature biases are important for understanding the  
390 simulations and predictions of global energy and heat redistribution.  
391 Though being substantial in climate simulations, subsurface biases have  
392 not been received much attention yet. In this study, subsurface temperature  
393 biases in the TNP are investigated using the newly released CMIP6  
394 historical simulations. It is found that almost all the CMIP6 simulations  
395 have a pronounced SWB that is persistent throughout the year in the NETP,  
396 and the model updates from CMIP5 to CMIP6 do not provide obvious bias  
397 alleviations for temperature biases. The SWB is primarily caused by the  
398 model deficiencies in simulating the surface WSC. For a similar reason,  
399 the poorly prescribed wind forcing also causes a pronounced SWB in the  
400 NETP in OMIP simulations. Besides, this SWB can also be partly  
401 attributed to the uncertainties in the representations of the oceanic vertical  
402 mixing processes. Compared with the observations, the estimated vertical  
403 diffusivity in ocean model is misrepresented in both the upper boundary  
404 layer and the ocean interior. By constraining the diffusivity to match  
405 observations, SWB in the NETP is reduced by  $\sim 3$  °C. The consequence of  
406 the SWB in the NETP is further examined using the CMIP6 products. The  
407 SWB can influence the simulations of oceanic circulations and equatorial

408 upper-ocean thermal structure. The CMIP6 simulations with a large SWB  
409 tend to produce a weak equatorward water transport in the subsurface TNP,  
410 a weak equatorial upwelling and thus a warm upper ocean layer along the  
411 equator.

412 Substantial subsurface temperature biases are also seen in other  
413 regions of the world ocean (Fig. 15a). Unfortunately, it seems that no  
414 substantial improvements are achieved from CMIP5 to CMIP6 (Fig. 15b),  
415 and much more efforts are needed to understand the sources of subsurface  
416 biases and ultimately to remove them. It is interesting to note that the  
417 subsurface temperature bias is often accompanied by a bias in salinity  
418 simulation, and the biases in temperature and salinity are compensated for  
419 by each other in terms of their effects on density. For example, the large  
420 subsurface cold bias centered at (the Pacific sector, 8° S, 200 m) is  
421 accompanied by a fresh bias. Because these two biases tend to be  
422 compensated for by each other in terms of their effects on density, density  
423 bias is reduced. Compensation of temperature and salinity is a property  
424 commonly observed in water masses (Lilly et al., 1999; Rudnick and  
425 Ferrari, 1999). Thus, subsurface thermohaline biases might be closely  
426 related to the water mass formation and transformation in the global oceans.

427 Figure 14 shows a positive correlation between the SWB and the  
428 equatorial upper-ocean temperature in CMIP6 models. Previous studies  
429 have found that the cold bias in the upper tropical Pacific Ocean affects the

430 ENSO simulations in climate models, leading to an intermodel diversity of  
431 ENSO representations in CMIP5 simulations (Vannière et al., 2013; Kim  
432 et al., 2014). The upper ocean temperature bias in the equatorial Pacific is  
433 a possible cause of forecast errors in ENSO amplitude (Kim et al., 2017).  
434 Thus, the SWB might be linked to the ENSO simulations in climate models,  
435 and further research efforts are needed to test this hypothesis.

436

437 ***Acknowledgement.***

438 We thank Andreas M. Thurnherr at Lamont-Doherty Earth Observatory for  
439 providing the LADDER data. We acknowledge the World Climate  
440 Research Programme, which, through its Working Group on Coupled  
441 Modelling, coordinated and promoted CMIP6. We thank the climate  
442 modeling groups for producing and making available their model output,  
443 the Earth System Grid Federation (ESGF) for archiving the data and  
444 providing access, and the multiple funding agencies who support CMIP6  
445 and ESGF. This research is supported by the National Natural Science  
446 Foundation of China (Grant Nos. 41906007, 41690122(41690120),  
447 42030410, 41705082, 41421005), the National Key Research and  
448 Development Program of China (No.  
449 2017YFC1404102(2017YFC1404100)), the Strategic Priority Research  
450 Program of Chinese Academy of Sciences (Grant Nos. XDB 40000000 and  
451 XDB 42000000), and the Shandong Taishan Scholarship.

452

453 **References**

454 Acreman, D. M., and C. D. Jeffery, 2007: The use of Argo for validation  
455 and tuning of mixed layer models. *Ocean Modell.*, **19**, 53-69.

456 Burls, N. J., L. Muir, E. M. Vincent, and A. Fedorov, 2017: Extra-tropical  
457 origin of equatorial Pacific cold bias in climate models with links to  
458 cloud albedo. *Clim. Dyn.*, **49**, 2093-2113.

459 Capotondi, A., M. A. Alexander, C. Deser, and M. J. McPhaden, 2005:  
460 Anatomy and Decadal Evolution of the Pacific Subtropical–Tropical  
461 Cells (STCs)\*. *J. Climate*, **18**, 3739-3758.

462 Chen, D., L. M. Rothstein, and A. J. Busalacchi, 1994: A Hybrid Vertical  
463 Mixing Scheme and Its Application to Tropical Ocean Models. *J.*  
464 *Phys. Oceanogr.*, **24**, 2156-2179.

465 Chen, X. Y., and K. K. Tung, 2014: Varying planetary heat sink led to  
466 global-warming slowdown and acceleration. *Science*, **345**, 897-903.

467 Cheng, L., and Y. Kitade, 2014: Quantitative evaluation of turbulent  
468 mixing in the Central Equatorial Pacific. *J. Oceanogr.*, **70**, 63-79.

469 Chowdary, J. S., A. Parekh, G. Srinivas, C. Gnanaseelan, T. S. Fousiya, R.  
470 Khandekar, and M. K. Roxy, 2016: Processes Associated with the  
471 Tropical Indian Ocean Subsurface Temperature Bias in a Coupled  
472 Model. *J. Phys. Oceanogr.*, **46**, 2863-2875.

473 Copernicus Climate Change Service (C3S), 2017: ERA5: Fifth generation

474 of ECMWF atmospheric reanalyses of the global climate. *Copernicus*  
475 *Climate Change Service Climate Data Store (CDS)*, 2019/04/24.  
476 <https://cds.climate.copernicus.eu/cdsapp#!/home>.

477 Draper, D. W., and D. G. Long, 2004: Evaluating the effect of rain on  
478 SeaWinds scatterometer measurements. *J. Geophys. Res.*, **109**,  
479 C02005.

480 Eyring, V., S. Bony, G. A. Meehl, C. A. Senior, B. Stevens, R. J. Stouffer,  
481 and K. E. Taylor, 2016: Overview of the Coupled Model  
482 Intercomparison Project Phase 6 (CMIP6) experimental design and  
483 organization. *Geosci. Model Dev.*, **9**, 1937-1958.

484 Fernández-Castro, B., and Coauthors, 2014: Microstructure turbulence and  
485 diffusivity parameterization in the tropical and subtropical Atlantic,  
486 Pacific and Indian Oceans during the Malaspina 2010 expedition.  
487 *Deep Sea Research Part I: Oceanographic Research Papers*, **94**, 15-  
488 30.

489 Furue, R., and Coauthors, 2015: Impacts of regional mixing on the  
490 temperature structure of the equatorial Pacific Ocean. Part 1:  
491 Vertically uniform vertical diffusion. *Ocean Modell.*, **91**, 91-111.

492 Gao, C., and R.-H. Zhang, 2017: The roles of atmospheric wind and  
493 entrained water temperature ( $T_e$ ) in the second-year cooling of the  
494 2010–12 La Niña event. *Clim. Dyn.*, **48**, 597-617.

495 Good, S. A., M. J. Martin, and N. A. Rayner, 2013: EN4: Quality controlled

496 ocean temperature and salinity profiles and monthly objective  
497 analyses with uncertainty estimates. *J. Geophys. Res.*, **118**, 6704-6716.

498 Gordon, C. T., A. Rosati, and R. Gudgel, 2000: Tropical Sensitivity of a  
499 Coupled Model to Specified ISCCP Low Clouds. *J. Climate*, **13**,  
500 2239-2260.

501 Griffies, S. M., and Coauthors, 2009: Coordinated Ocean-ice Reference  
502 Experiments (COREs). *Ocean Modell.*, **26**, 1-46.

503 Griffies, S. M., and Coauthors, 2015: Impacts on Ocean Heat from  
504 Transient Mesoscale Eddies in a Hierarchy of Climate Models. *J.*  
505 *Climate*, **28**, 952-977.

506 Griffies, S. M., and Coauthors, 2016: OMIP contribution to CMIP6:  
507 experimental and diagnostic protocol for the physical component of  
508 the Ocean Model Intercomparison Project. *Geosci. Model Dev.*, **9**,  
509 3231-3296.

510 Guilyardi, E., and Coauthors, 2009: Understanding El Niño in Ocean–  
511 Atmosphere General Circulation Models: Progress and Challenges.  
512 *Bull. Amer. Meteor. Soc.*, **90**, 325-340.

513 Jia, Y. L., R. Furue, and J. P. McCreary, 2015: Impacts of regional mixing  
514 on the temperature structure of the equatorial Pacific Ocean. Part 2:  
515 Depth-dependent vertical diffusion. *Ocean Modell.*, **91**, 112-127.

516 Jochum, M., 2009: Impact of latitudinal variations in vertical diffusivity on  
517 climate simulations. *J. Geophys. Res.*, **114**, C01010.

518 Johnson, G. C., and M. J. McPhaden, 1999: Interior Pycnocline Flow from  
519 the Subtropical to the Equatorial Pacific Ocean. *J. Phys. Oceanogr.*,  
520 **29**, 3073-3089.

521 Kim, S. T., H.-I. Jeong, and F.-F. Jin, 2017: Mean Bias in Seasonal Forecast  
522 Model and ENSO Prediction Error. *Sci. Rep.*, **7**, 6029.

523 Kim, S. T., W. Cai, F.-F. Jin, and J.-Y. Yu, 2014: ENSO stability in coupled  
524 climate models and its association with mean state. *Clim. Dyn.*, **42**,  
525 3313-3321.

526 Kunze, E., E. Firing, J. M. Hummon, T. K. Chereskin, and A. M. Thurnherr,  
527 2006: Global Abyssal Mixing Inferred from Lowered ADCP Shear  
528 and CTD Strain Profiles. *J. Phys. Oceanogr.*, **36**, 1553-1576.

529 Large, W. G., and S. G. Yeager, 2009: The global climatology of an  
530 interannually varying air-sea flux data set. *Clim. Dyn.*, **33**, 341-364.

531 Li, G., S.-P. Xie, Y. Du, and Y. Luo, 2016: Effects of excessive equatorial  
532 cold tongue bias on the projections of tropical Pacific climate change.  
533 Part I: the warming pattern in CMIP5 multi-model ensemble. *Clim.*  
534 *Dyn.*, **47**, 3817-3831.

535 Lilly, J. M., P. B. Rhines, M. Visbeck, R. Davis, J. R. N. Lazier, F. Schott,  
536 and D. Farmer, 1999: Observing Deep Convection in the Labrador  
537 Sea during Winter 1994/95 %J Journal of Physical Oceanography. *J.*  
538 *Phys. Oceanogr.*, **29**, 2065-2098.

539 Lu, P., and J. P. McCreary, 1995: Influence of the ITCZ on the Flow of

540 Thermocline Water from the Subtropical to the Equatorial Pacific  
541 Ocean. *J. Phys. Oceanogr.*, **25**, 3076-3088.

542 Ma, C.-C., C. R. Mechoso, A. W. Robertson, and A. Arakawa, 1996:  
543 Peruvian Stratus Clouds and the Tropical Pacific Circulation: A  
544 Coupled Ocean-Atmosphere GCM Study. *J. Climate*, **9**, 1635-1645.

545 McPhaden, M. J., and D. Zhang, 2002: Slowdown of the meridional  
546 overturning circulation in the upper Pacific Ocean. *Nature*, **415**, 603-  
547 608.

548 Niiler, P., 1977: One-dimensional models of the upper ocean, Modelling  
549 and Prediction of the Upper Layers of the Ocean EB Kraus, 143–172.  
550 Pergamon, New York.

551 Peters, H., M. C. Gregg, and J. M. Toole, 1988: On the parameterization of  
552 equatorial turbulence. *J. Geophys. Res.*, **93**, 1199-1218.

553 Rackow, T., and Coauthors, 2019: Sensitivity of deep ocean biases to  
554 horizontal resolution in prototype CMIP6 simulations with AWI-  
555 CM1.0. *Geosci. Model Dev.*, **12**, 2635-2656.

556 Risien, C. M., and D. B. Chelton, 2008: A Global Climatology of Surface  
557 Wind and Wind Stress Fields from Eight Years of QuikSCAT  
558 Scatterometer Data. *J. Phys. Oceanogr.*, **38**, 2379-2413.

559 Rothstein, L. M., R.-H. Zhang, A. J. Busalacchi, and D. Chen, 1998: A  
560 Numerical Simulation of the Mean Water Pathways in the Subtropical  
561 and Tropical Pacific Ocean. *J. Phys. Oceanogr.*, **28**, 322-343.

562 Rudnick, D. L., and R. Ferrari, 1999: Compensation of Horizontal  
563 Temperature and Salinity Gradients in the Ocean Mixed Layer.  
564 *Science*, **283**, 526-529.

565 Sasaki, W., K. J. Richards, and J. J. Luo, 2013: Impact of vertical mixing  
566 induced by small vertical scale structures above and within the  
567 equatorial thermocline on the tropical Pacific in a CGCM. *Clim. Dyn.*,  
568 **41**, 443-453.

569 Seo, H., M. Jochum, R. Murtugudde, and A. J. Miller, 2006: Effect of ocean  
570 mesoscale variability on the mean state of tropical Atlantic climate.  
571 *Geophys. Res. Lett.*, **33**, L09606.

572 Small, R. J., and Coauthors, 2014: A new synoptic scale resolving global  
573 climate simulation using the Community Earth System Model. *J. Adv.*  
574 *Model. Earth Syst.*, **6**, 1065-1094.

575 Song, F., and G. J. Zhang, 2020: The Impacts of Horizontal Resolution on  
576 the Seasonally Dependent Biases of the Northeastern Pacific ITCZ in  
577 Coupled Climate Models. *J. Climate*, **33**, 941-957.

578 Sun, Z., H. Liu, P. Lin, Y.-h. Tseng, J. Small, and F. Bryan, 2019: The  
579 Modeling of the North Equatorial Countercurrent in the Community  
580 Earth System Model and its Oceanic Component. *Journal of*  
581 *Advances in Modeling Earth Systems*, **11**, 531-544.

582 Thomas, M. D., and A. V. Fedorov, 2017: The Eastern Subtropical Pacific  
583 Origin of the Equatorial Cold Bias in Climate Models: A Lagrangian

584           Perspective. *J. Climate*, **30**, 5885-5900.

585   Tsujiro, H., and Coauthors, 2018: JRA-55 based surface dataset for driving  
586           ocean–sea-ice models (JRA55-do). *Ocean Modell.*, **130**, 79-139.

587   Vannière, B., E. Guilyardi, G. Madec, F. J. Doblas-Reyes, and S.  
588           Woolnough, 2013: Using seasonal hindcasts to understand the origin  
589           of the equatorial cold tongue bias in CGCMs and its impact on ENSO.  
590           *Clim. Dyn.*, **40**, 963-981.

591   Wang, G., L. Cheng, J. Abraham, and C. Li, 2018: Consensuses and  
592           discrepancies of basin-scale ocean heat content changes in different  
593           ocean analyses. *Clim. Dyn.*, **50**, 2471-2487.

594   Weissman, D. E., M. A. Bourassa, and J. Tongue, 2002: Effects of Rain  
595           Rate and Wind Magnitude on SeaWinds Scatterometer Wind Speed  
596           Errors. *J. Atmos. Oceanic Technol.*, **19**, 738-746.

597   Wittenberg, A. T., A. Rosati, N.-C. Lau, and J. J. Ploshay, 2006: GFDL's  
598           CM2 Global Coupled Climate Models. Part III: Tropical Pacific  
599           Climate and ENSO. *J. Climate*, **19**, 698-722.

600   Woelfle, M. D., S. Yu, C. S. Bretherton, and M. S. Pritchard, 2018:  
601           Sensitivity of Coupled Tropical Pacific Model Biases to Convective  
602           Parameterization in CESM1. *J. Adv. Model. Earth Syst.*, **10**, 126-144.

603   Xu, Z., M. Li, C. M. Patricola, and P. Chang, 2014: Oceanic origin of  
604           southeast tropical Atlantic biases. *Clim. Dyn.*, **43**, 2915-2930.

605   Ying, J., P. Huang, T. Lian, and H. Tan, 2019: Understanding the effect of

606 an excessive cold tongue bias on projecting the tropical Pacific SST  
607 warming pattern in CMIP5 models. *Clim. Dyn.*, **52**, 1805-1818.

608 Zhang, R.-H., and Coauthors, 2020: A review of progress in coupled ocean-  
609 atmosphere model developments for ENSO studies in China. *Journal*  
610 *of Oceanology and Limnology*, **38**, 930-961.

611 Zhu, C., Z. Liu, and S. Gu, 2018: Model bias for South Atlantic Antarctic  
612 intermediate water in CMIP5. *Clim. Dyn.*, **50**, 3613-3624.

613 Zhu, Y., and R.-H. Zhang, 2018a: Scaling wind stirring effects in an  
614 oceanic bulk mixed layer model with application to an OGCM of the  
615 tropical Pacific. *Clim. Dyn.*, **51**, 1927-1946.

616 Zhu, Y., and R.-H. Zhang, 2018b: An Argo-Derived Background  
617 Diffusivity Parameterization for Improved Ocean Simulations in the  
618 Tropical Pacific. *Geophys. Res. Lett.*, **45**, 1509-1517.

619 Zhu, Y., and R.-H. Zhang, 2019: A Modified Vertical Mixing  
620 Parameterization for Its Improved Ocean and Coupled Simulations in  
621 the Tropical Pacific. *J. Phys. Oceanogr.*, **49**, 21-37.

622 Zhu, Y., R.-H. Zhang, and J. Sun, 2020a: North Pacific Upper-Ocean Cold  
623 Temperature Biases in CMIP6 Simulations and the Role of Regional  
624 Vertical Mixing. *J. Climate*, **33**, 7523-7538.

625 Zhu, Y., R.-H. Zhang, D. Li, and D. Chen, 2020b: The thermocline biases  
626 in the tropical North Pacific and their attributions. *J. Climate*, 1-17.

627 Retrieved Dec 15, 2020, from

628 [https://journals.ametsoc.org/view/journals/clim/aop/JCLI-D-20-](https://journals.ametsoc.org/view/journals/clim/aop/JCLI-D-20-0675.1/JCLI-D-20-0675.1.xml)

629 [0675.1/JCLI-D-20-0675.1.xml](https://journals.ametsoc.org/view/journals/clim/aop/JCLI-D-20-0675.1/JCLI-D-20-0675.1.xml)

630

631 **Declarations**

632 **Funding**

633 This research is supported by the National Natural Science  
634 Foundation of China (Grant Nos. 41906007, 41690122(41690120),  
635 42030410, 41705082, 41421005), the National Key Research and  
636 Development Program of China (No.  
637 2017YFC1404102(2017YFC1404100)), the Strategic Priority Research  
638 Program of Chinese Academy of Sciences (Grant Nos. XDB 40000000 and  
639 XDB 42000000), and the Shandong Taishan Scholarship.

640 **Conflicts of interest/Competing interests**

641 The authors declare no competing interests.

642 **Availability of data and material**

643 Not applicable.

644 **Code availability**

645 The data and computer codes used in the paper are available from the  
646 corresponding author (e-mail: [rzhang@qdio.ac.cn](mailto:rzhang@qdio.ac.cn)).

647

648 **Legends**

649 **Table 1.** CMIP and OMIP models used in this study.

650 **Figure 1.** (a) Spatial distributions of multimodel annual mean bias greater  
651 than 3 °C. (b) Subsurface temperature bias in the individual CMIP6 models,  
652 which is calculated by averaging the temperature bias over the region  
653 where the multimodel mean bias is greater than 3 °C. The x-axis denotes  
654 the model numbers, which are listed in Table 1.

655 **Figure 2.** The same as in Figure 1a but for the subsurface warm bias in  
656 CMIP5 multimodel ensemble.

657 **Figure 3.** Seasonal variation in the SWB, which is the horizontally  
658 averaged over the region (8°-15° N, 110°-150° W). The 20 °C isotherm  
659 depth from the EN4 is denoted by the solid line, and that from the CMIP6  
660 MME is denoted as the dashed line.

661 **Figure 4.** (a) Linear regression of the inter-model WSC [ $\text{N m}^{-3}$ ] onto the  
662 normalized series of SWB (Fig. 1b). The dots denote the region where P-  
663 value is smaller than 0.05. (b, c) WSC bias relative to ERA5 and SCOW,  
664 respectively.

665 **Figure 5.** (a) SWB [ $^{\circ}\text{C}$ ] at the depth of 100 m in the OMIP MME. (b) The  
666 WSC difference [ $\text{N m}^{-3}$ ] between the OMIP MME and the ERA5.

667 **Figure 6.** (a) Temperature bias at the depth of 100 m and (b) the vertical-  
668 season section of temperature bias horizontally averaged over the NETP in  
669 the LY09 run. (c, d) The differences between the ERA5 run and the LY09

670 run.

671 **Figure 7.** Linear regressions of the intermodel sea level pressure [color, Pa]  
672 and wind stress vectors [ $\text{N m}^{-2}$ ] onto the normalized SWB.

673 **Figure 8.** Base-10 logarithm of the vertical diffusivity (the averaged over  
674 ( $8^{\circ}$ - $15^{\circ}$  N,  $110^{\circ}$ - $150^{\circ}$  W),  $\text{m}^2 \text{s}^{-1}$ ) from the ocean-only experiment. Given  
675 the short period of the LY09 forcing fields (1948-2009), another OMIP-  
676 recommended forcing fields (Tsuji no et al., 2018) spanning 1958-2018 are  
677 used to drive the MOM5. Model outputs for the vertical diffusivity from  
678 2004-2012 are shown in colors, and three in-situ microstructure  
679 observations are indicated by the black lines.

680 **Figure 9.** (a) Microstructure profiles from the LADDER project (kindly  
681 provided by Professor Andreas M. Thurnherr at Lamont-Doherty Earth  
682 Observatory). These data were collected in the eastern tropical Pacific near  
683 the crest of the East Pacific Rise ( $9^{\circ}30'$ - $10^{\circ}$  N,  $103^{\circ}45'$ - $105^{\circ}$  W) using  
684 Vertical Microstructure Profiler (VMP) during November to December,  
685 2007. (b) The corresponding vertical diffusivity in MOM5 based ocean-  
686 only simulation.

687 **Figure 10.** Annual-mean differences in (a) ocean surface boundary layer  
688 [m] and (b) temperature at the depth of 100 m [ $^{\circ}\text{C}$ ] between the reduced  $m_0$   
689 run and the control run. (c) Vertical-season section of temperature  
690 difference horizontally averaged over the NETP.

691 **Figure 11.** (a) Diapycnal diffusivity estimated based on the finescale

692 parameterization using the Argo profiles (available online at  
693 <ftp://ftp.ifremer.fr/ifremer/argo/>) with 2-10 m vertical resolution and from  
694 2006 to 2019. (b, c) The temperature differences between the RBD run and  
695 the control run.

696 **Figure 12.** (a) Two model groups classified in terms of the SWB magnitude.  
697 Models in the Group1 have large SWB, while SWB in the Group2 is trivial.  
698 (c-d) Meridional velocity differences between the Group1 and Group2  
699 [colors,  $\text{cm s}^{-1}$ ], and potential density [ $\text{kg m}^{-3}$ ] in Group1 MME (solid lines)  
700 and Group2 MME (dashed lines) along  $5^\circ\text{N}$ ,  $10^\circ\text{N}$  and  $15^\circ\text{N}$ , respectively.

701 **Figure 13.** Vertical velocity [ $\text{m day}^{-1}$ ] along the equator in the (a) Group1  
702 MME and (b) Group2 MME. (c) The difference between Group1 and  
703 Group2.

704 **Figure 14.** (a) Temperature differences [ $^\circ\text{C}$ ] along the equator between the  
705 Group1 and Group2. (b) Scatterplots of the relationship between the SWB  
706 and the equatorial Pacific temperature averaged over (0-100 m,  $140^\circ\text{E}$ - $80^\circ$   
707  $\text{W}$ ).

708 **Figure 15.** The basinwide zonally averaged biases for temperature (colors)  
709 and salinity (contours) biases in (a) CMIP6 and (b) CMIP5.

710

# Figures

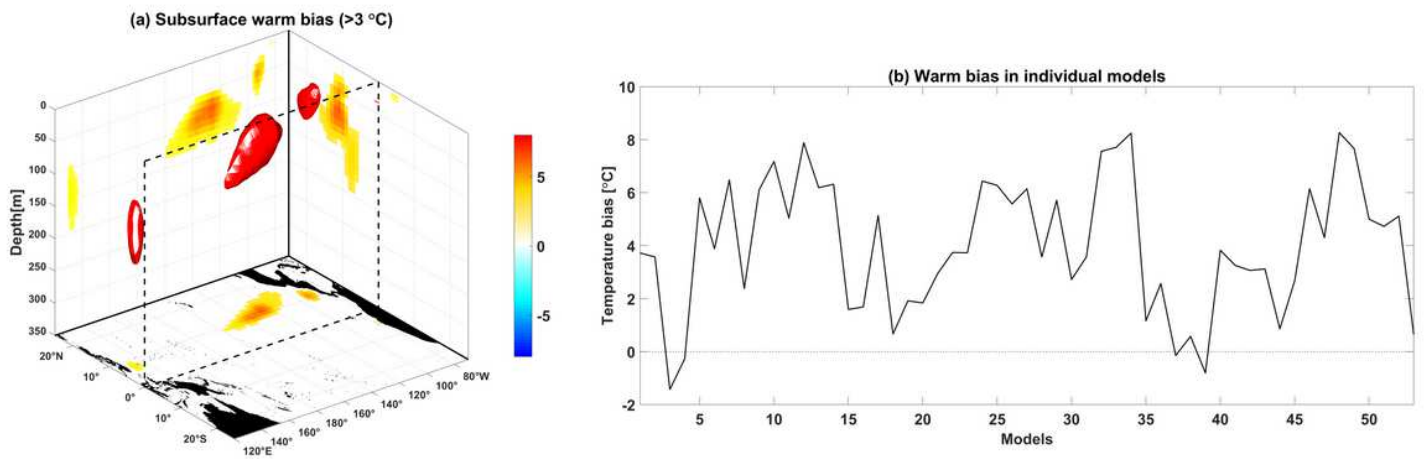


Figure 1

(a) Spatial distributions of multimodel annual mean bias greater than 3 °C. (b) Subsurface temperature bias in the individual CMIP6 models, which is calculated by averaging the temperature bias over the region where the multimodel mean bias is greater than 3 °C. The x-axis denotes the model numbers, which are listed in Table 1.

## Subsurface warm bias in CMIP5 ( $>3\text{ }^{\circ}\text{C}$ )

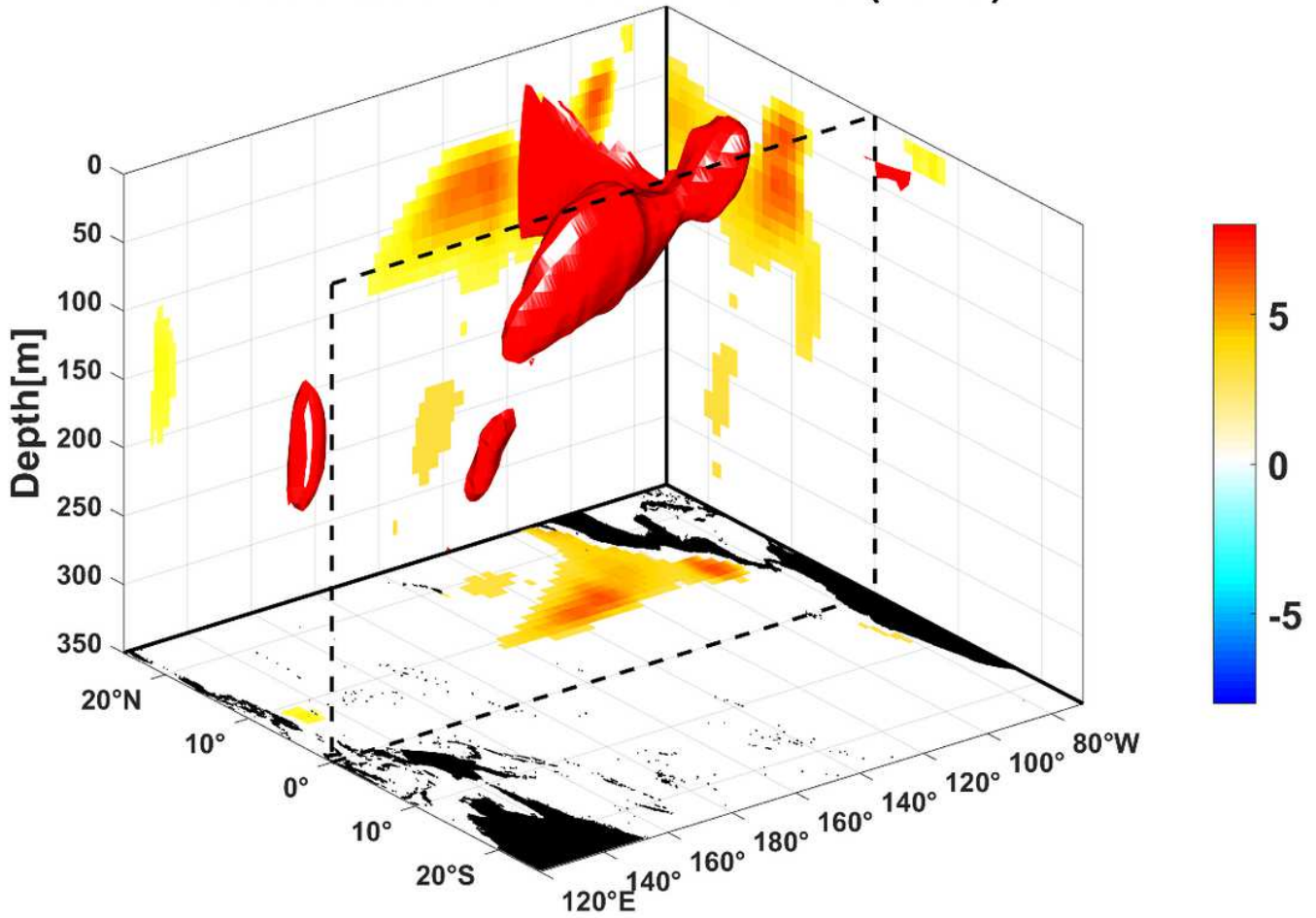
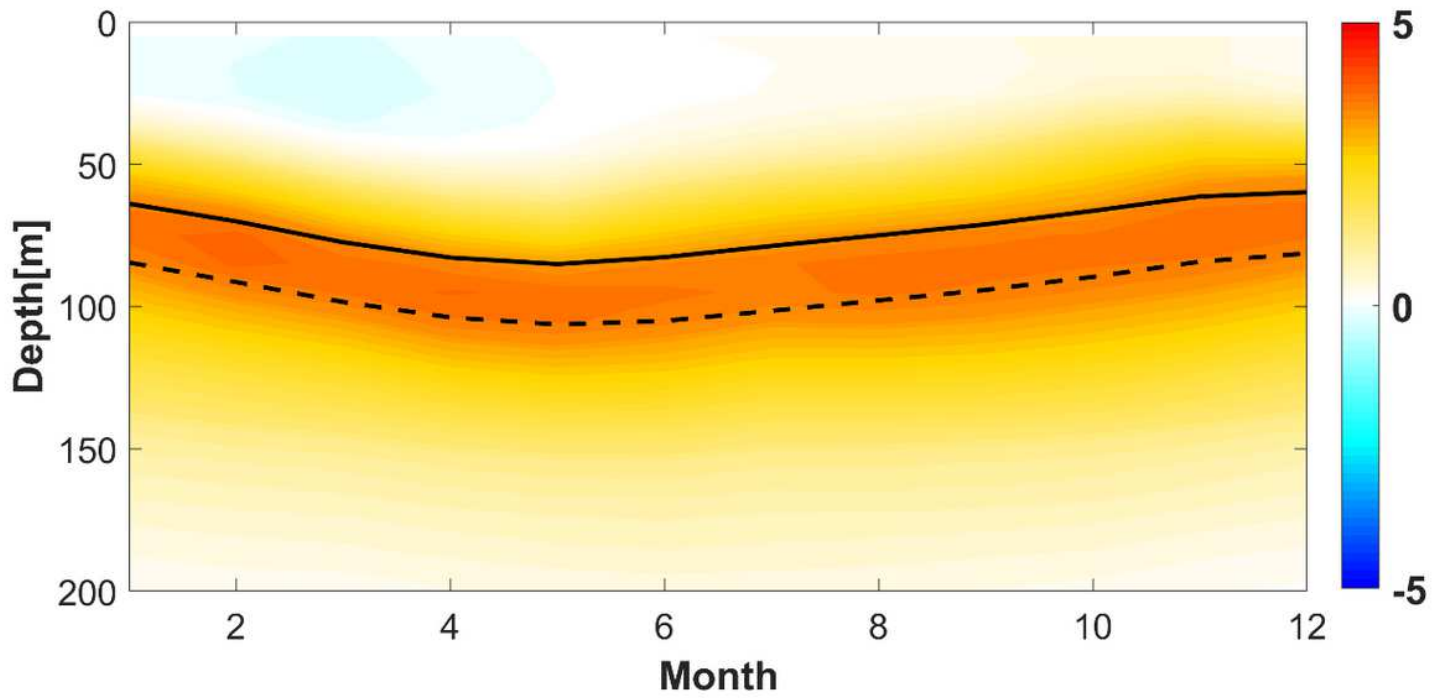


Figure 2

The same as in Figure 1a but for the subsurface warm bias in CMIP5 multimodel ensemble.



**Figure 3**

Seasonal variation in the SWB, which is the horizontally averaged over the region (8°-15° N, 110°-150° W). The 20 °C isotherm depth from the EN4 is denoted by the solid line, and that from the CMIP6 MME is denoted as the dashed line.

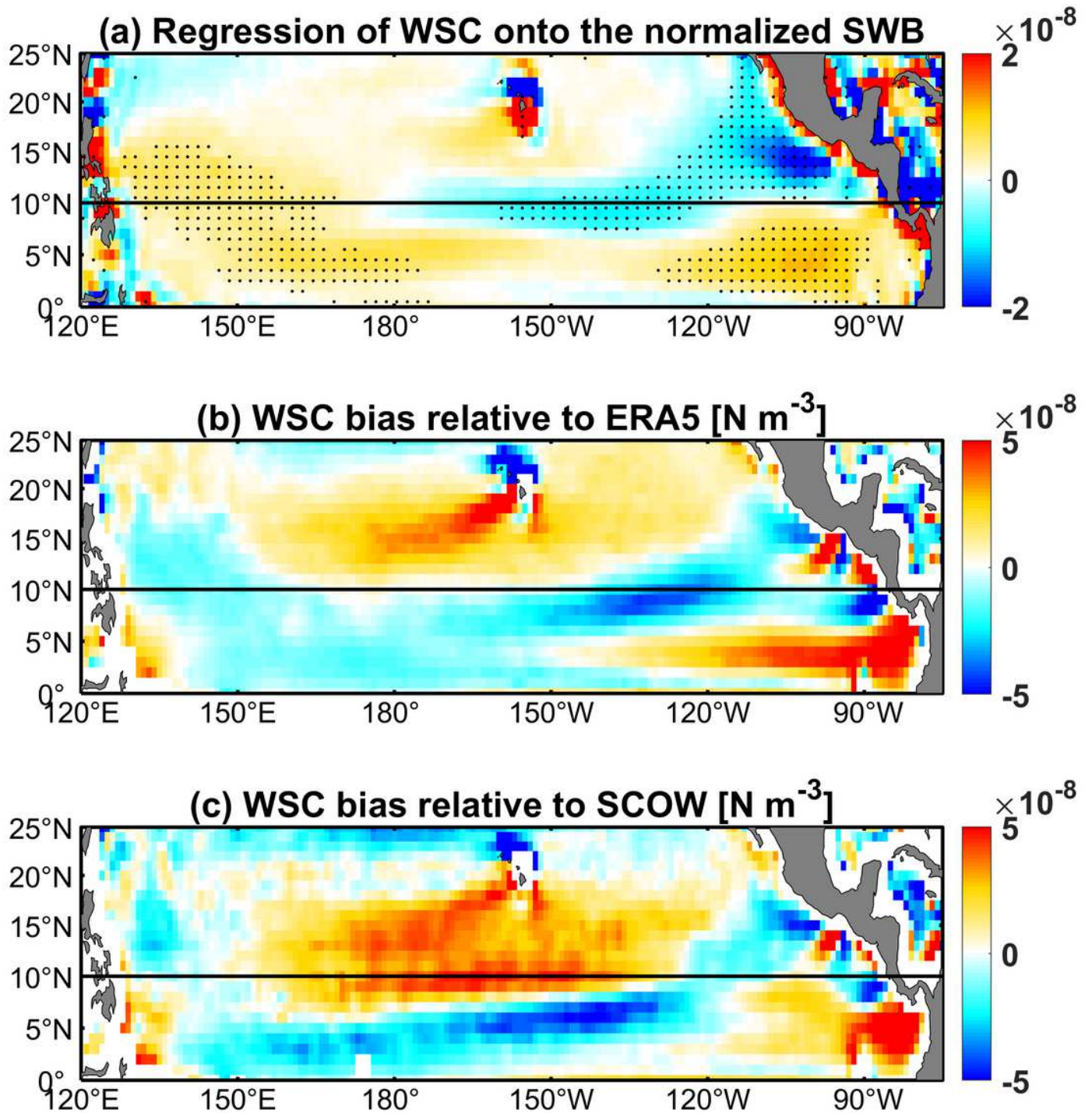


**Figure 4**

(a) Linear regression of the inter-model WSC [ $\text{N m}^{-3}$ ] onto the normalized series of SWB (Fig. 1b). The dots denote the region where P-value is smaller than 0.05. (b, c) WSC bias relative to ERA5 and SCOW, respectively.

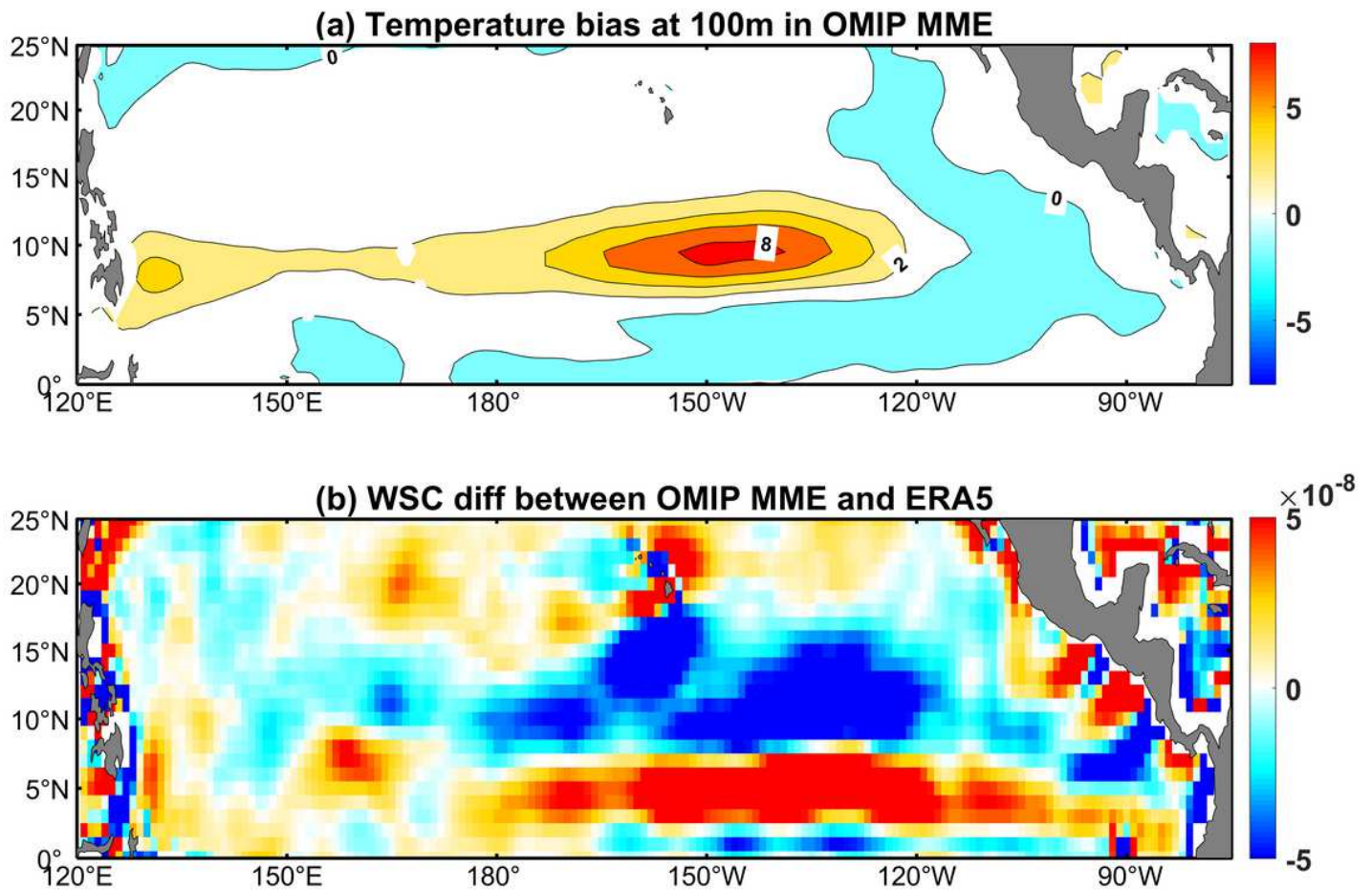


Figure 5

(a) SWB [ $^{\circ}\text{C}$ ] at the depth of 100 m in the OMIP MME. (b) The WSC difference [ $\text{N m}^{-3}$ ] between the OMIP MME and the ERA5.

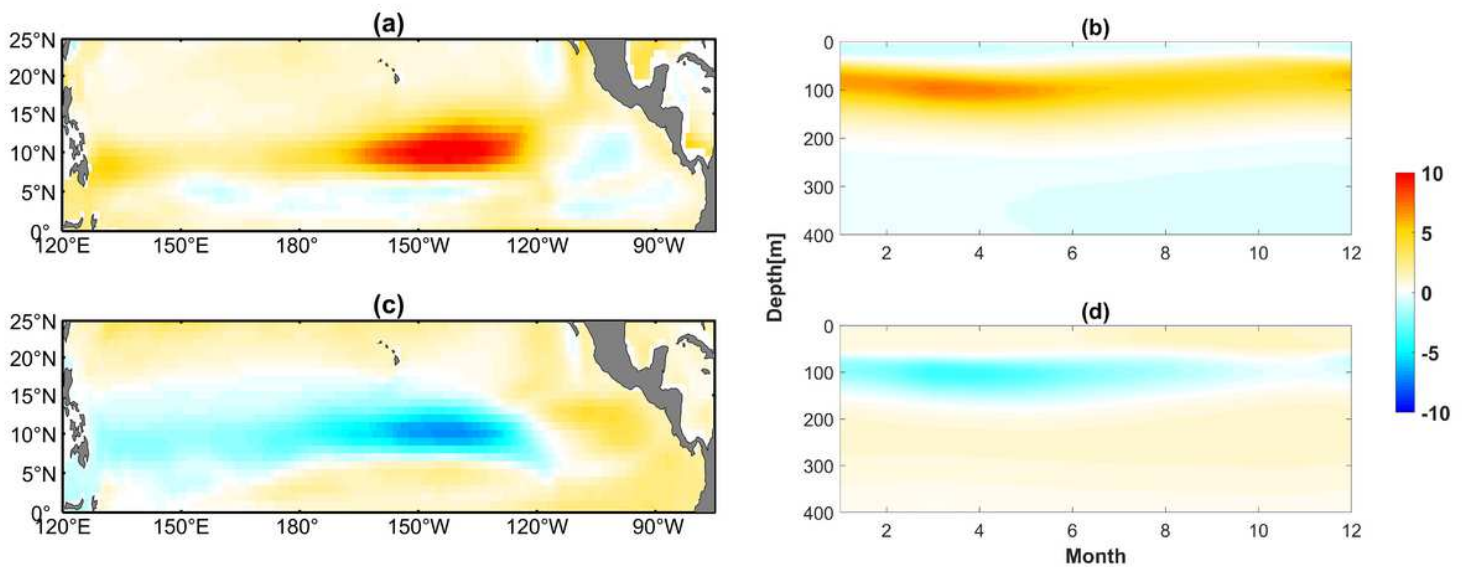
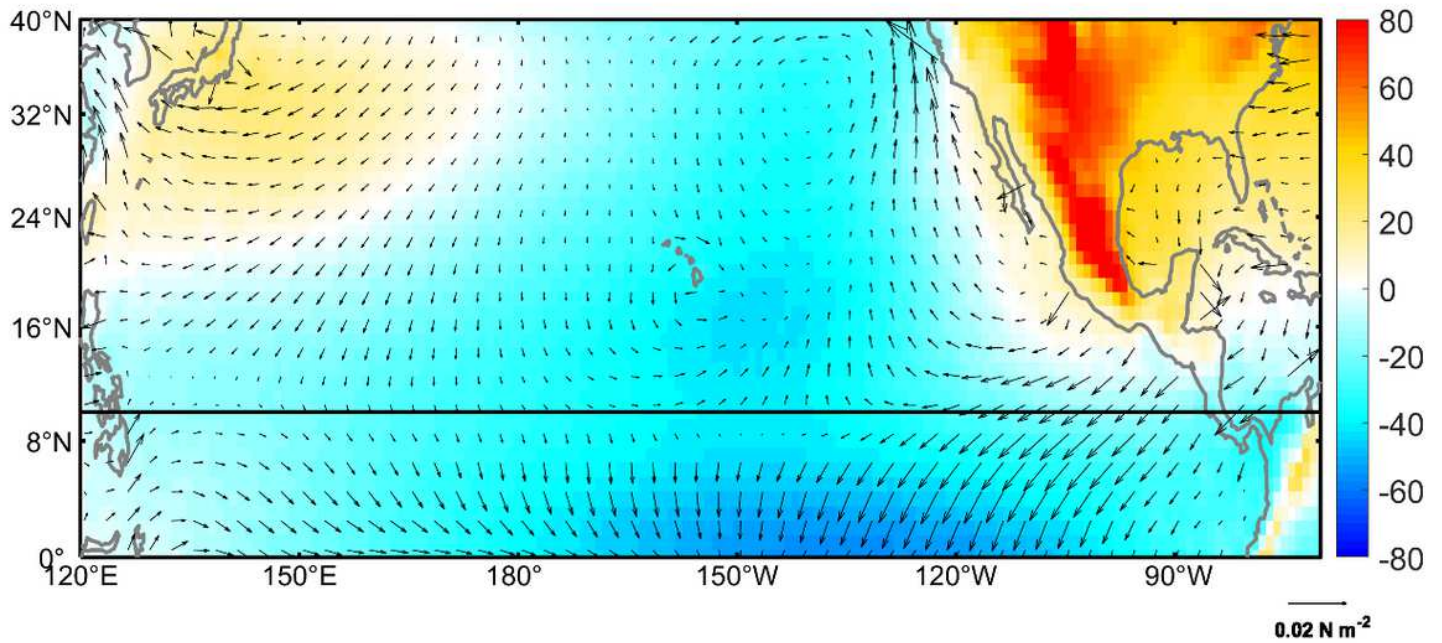


Figure 6

(a) Temperature bias at the depth of 100 m and (b) the vertical-season section of temperature bias horizontally averaged over the NETP in the LY09 run. (c, d) The differences between the ERA5 run and the LY09 run.



**Figure 7**

Linear regressions of the intermodel sea level pressure [color, Pa] and wind stress vectors [ $\text{N m}^{-2}$ ] onto the normalized SWB.

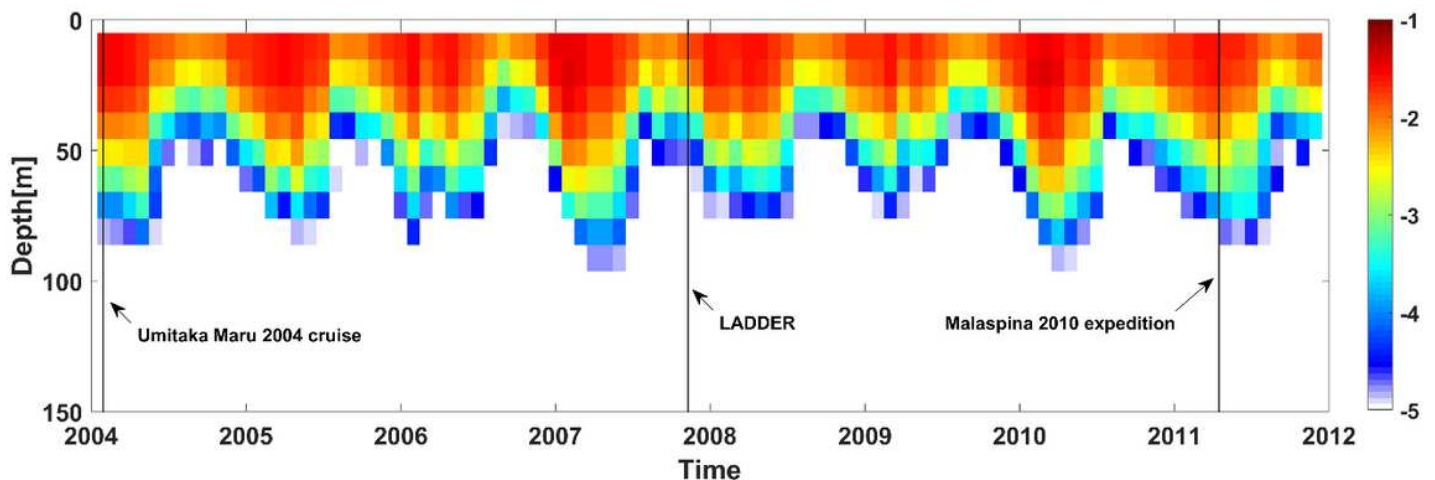


**Figure 8**

Base-10 logarithm of the vertical diffusivity (the averaged over  $(8^{\circ}\text{-}15^{\circ}\text{ N}, 110^{\circ}\text{-}150^{\circ}\text{ W})$ ,  $\text{m}^2\text{ s}^{-1}$ ) from the ocean-only experiment. Given the short period of the LY09 forcing fields (1948-2009), another OMIP-recommended forcing fields (Tsuji no et al., 2018) spanning 1958-2018 are used to drive the MOM5.

Model outputs for the vertical diffusivity from 2004-2012 are shown in colors, and three in-situ microstructure observations are indicated by the black lines.

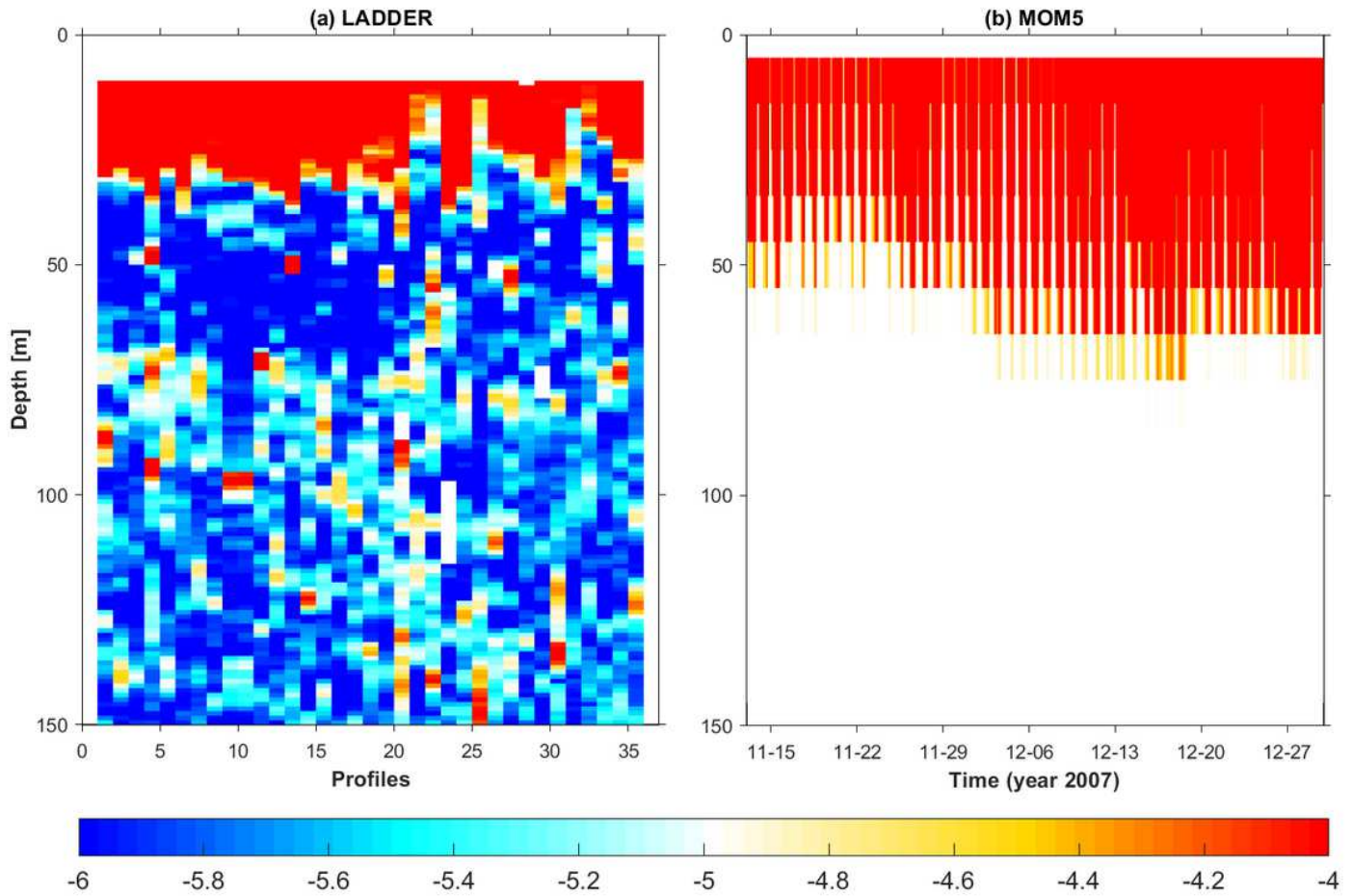


**Figure 9**

(a) Microstructure profiles from the LADDER project (kindly provided by Professor Andreas M. Thurnherr at Lamont-Doherty Earth Observatory). These data were collected in the eastern tropical Pacific near the crest of the East Pacific Rise ( $9^{\circ}30' - 10^{\circ}$  N,  $103^{\circ}45' - 105^{\circ}$  W) using Vertical Microstructure Profiler (VMP) during November to December, 2007. (b) The corresponding vertical diffusivity in MOM5 based ocean-only simulation.

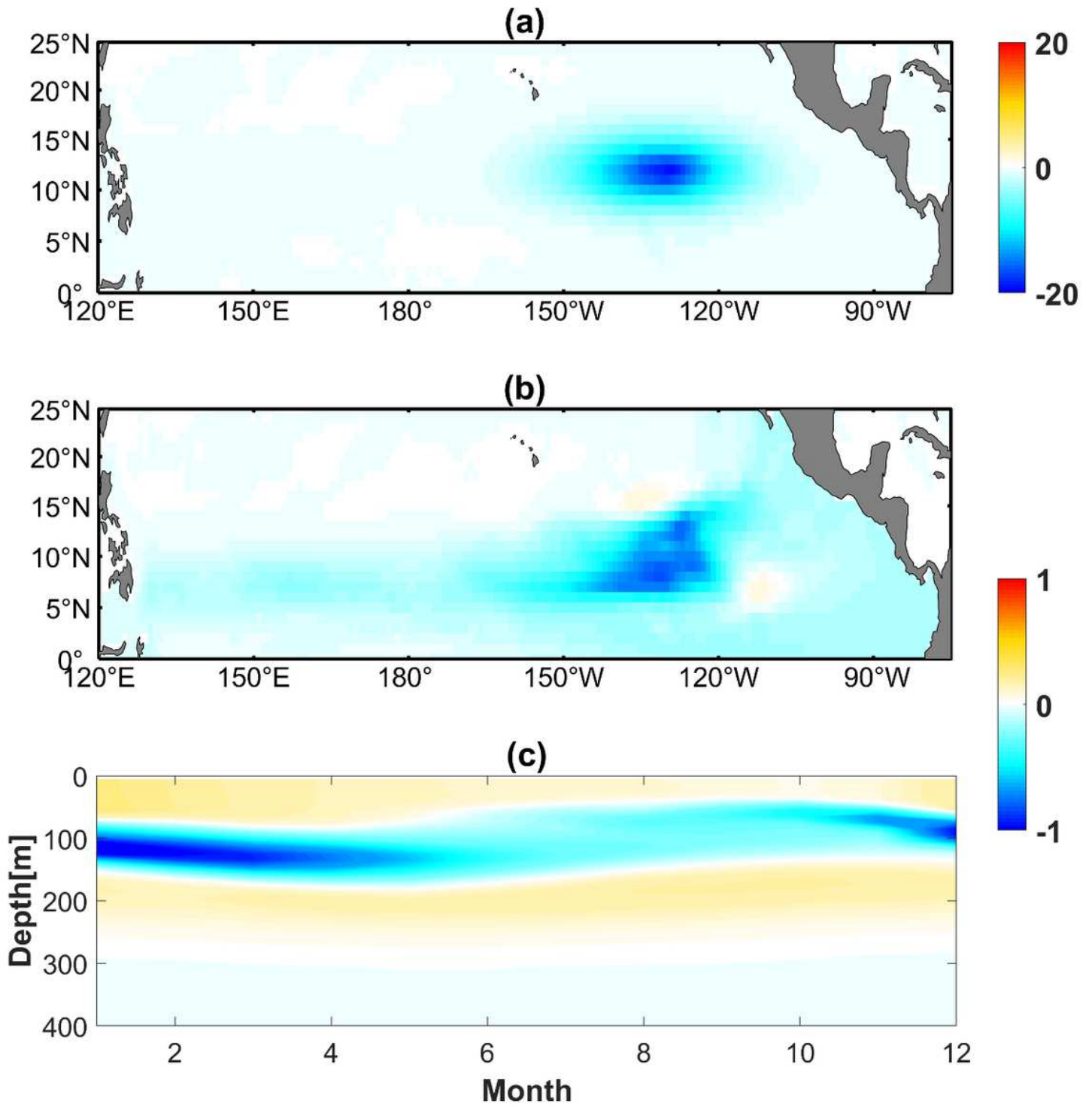


**Figure 10**

Annual-mean differences in (a) ocean surface boundary layer [m] and (b) temperature at the depth of 100 m [°C] between the reduced m0 run and the control run. (c) Vertical-season section of temperature difference horizontally averaged over the NETP.

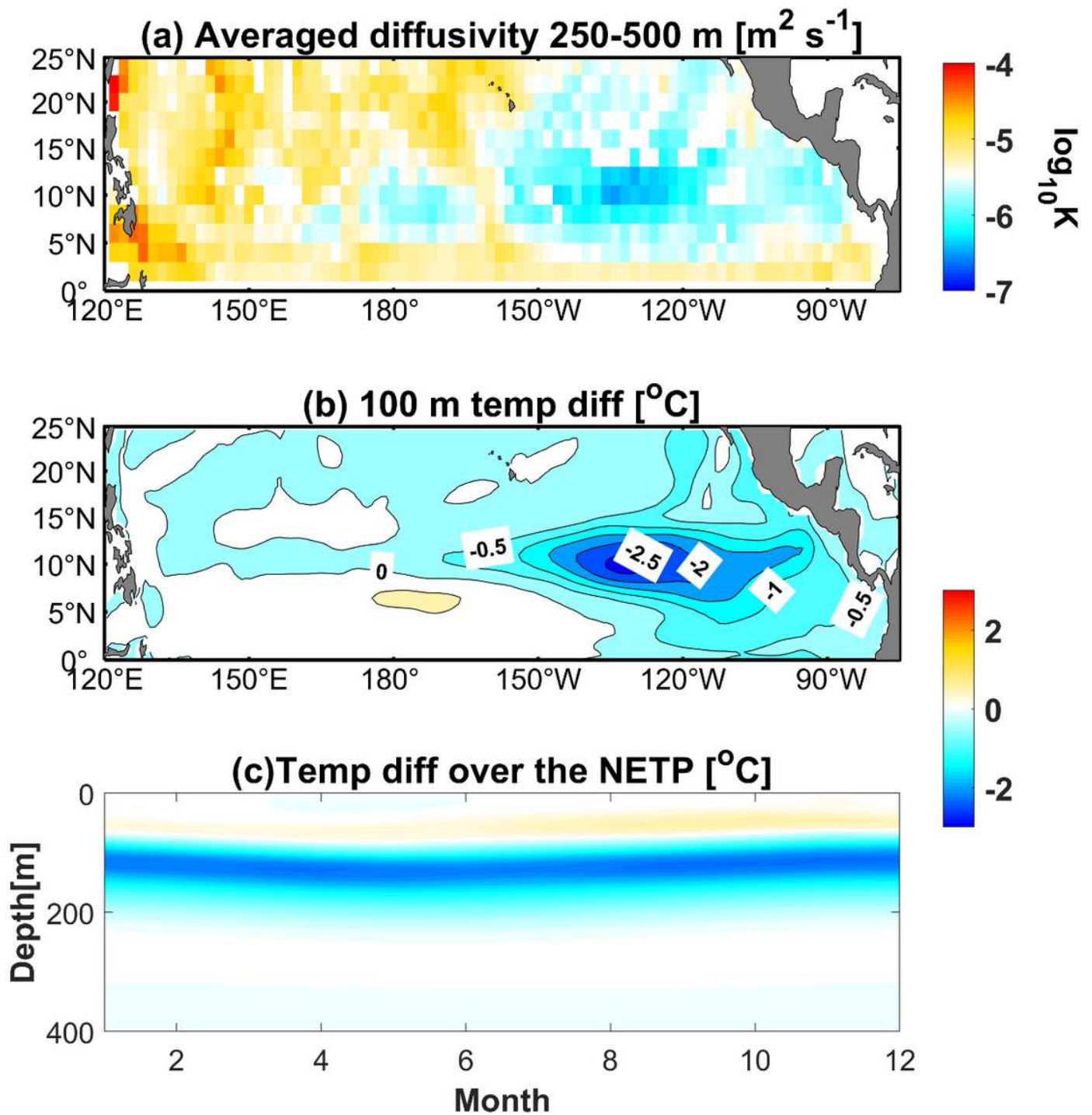


**Figure 11**

(a) Diapycnal diffusivity estimated based on the finescale parameterization using the Argo profiles (available online at <ftp://ftp.ifremer.fr/ifremer/argo/>) with 2-10 m vertical resolution and from 2006 to 2019. (b, c) The temperature differences between the RBD run and the control run.

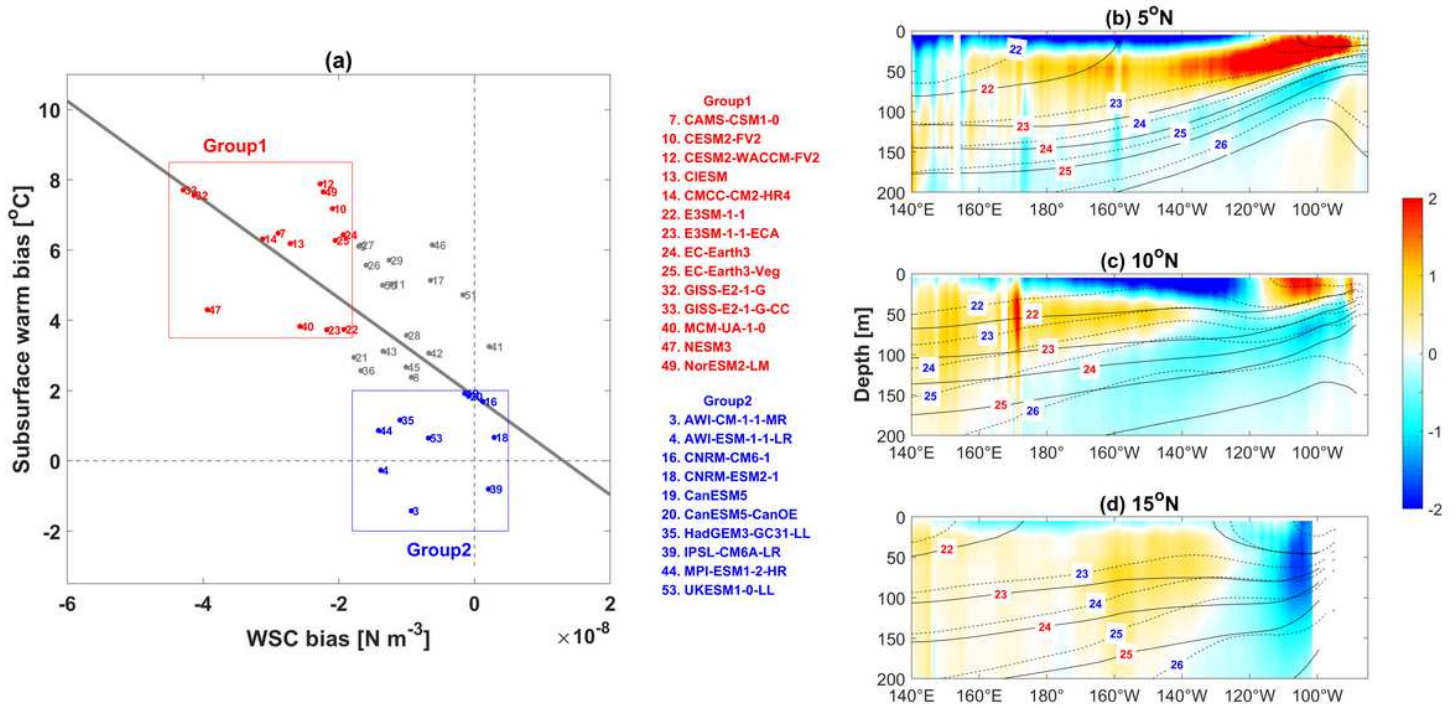


**Figure 12**

(a) Two model groups classified in terms of the SWB magnitude. Models in the Group1 have large SWB, while SWB in the Group2 is trivial. (c-d) Meridional velocity differences between the Group1 and Group2 [colors, cm s<sup>-1</sup>], and potential density [ $\text{kg m}^{-3}$ ] in Group1 MME (solid lines) and Group2 MME (dashed lines) along 5°N, 10°N and 15°N, respectively.

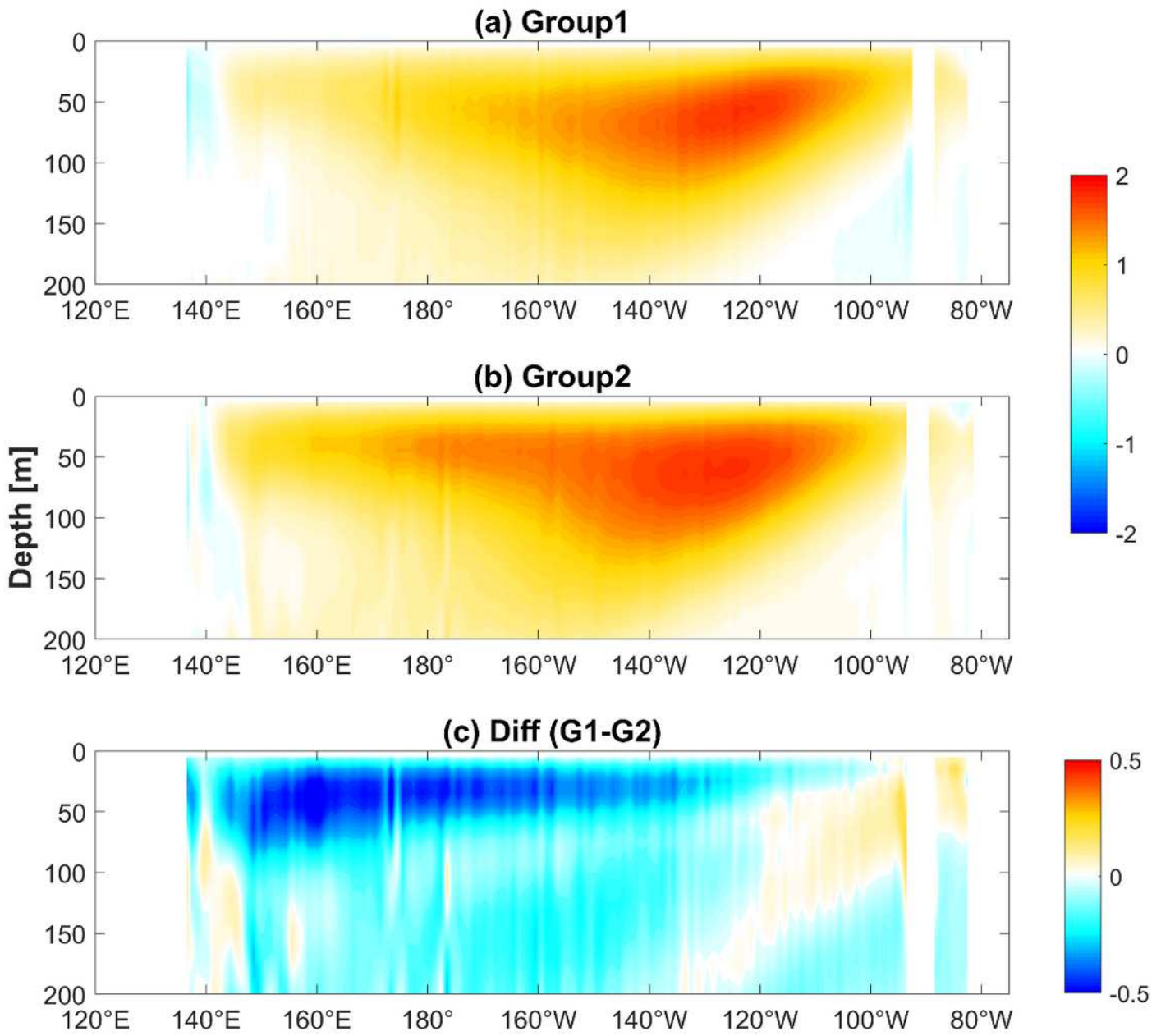


**Figure 13**

Vertical velocity [m day<sup>-1</sup>] along the equator in the (a) Group1 MME and (b) Group2 MME. (c) The difference between Group1 and Group2.

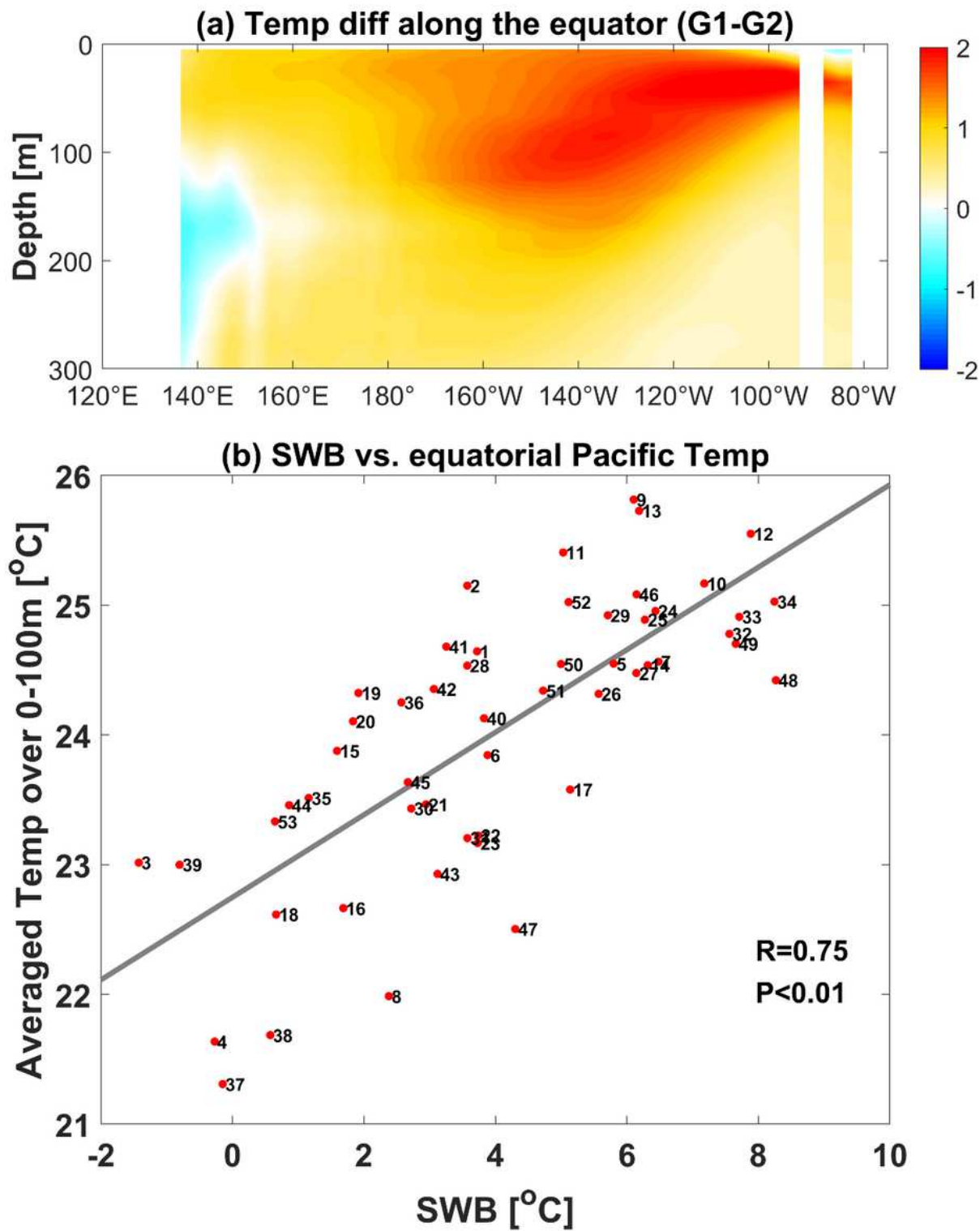
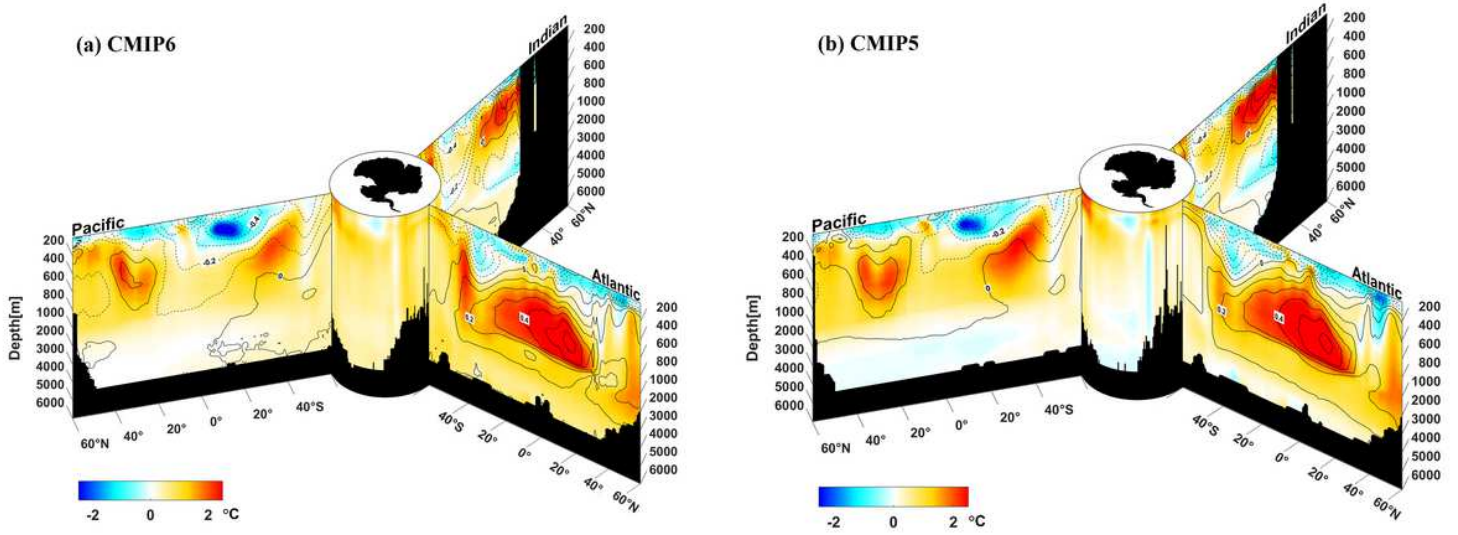


Figure 14

(a) Temperature differences [°C] along the equator between the Group1 and Group2. (b) Scatterplots of the relationship between the SWB and the equatorial Pacific temperature averaged over (0-100 m, 140° E-80° W).



Global distribution of thermohaline bias

Figure 15

The basinwide zonally averaged biases for temperature (colors) and salinity (contours) biases in (a) CMIP6 and (b) CMIP5.